Final Report on Optically Detected Magnetic Resonance Microscopy

Student: Hemanto Bairagi and Supervisor: Paul Barclay

University of Calgary, Department of Physics and Astrophysics

(Dated: March 25, 2020)

I. INTRODUCTION

The objective of this project, is to build a cost effective Optically detected magnetic resonance (ODMR) microscope, interface it with modern computer technology, and quantum experiments with the magnetic resonance microscope. The motivation to run this project, is that these quantum experiments will allow the improvement in modulating emitted intensities from NV containing diamonds, which will increase the ability for imaging applications to develop and improve [1, 2], thus advancing the field of ODMR. The quantum system used to run these quantum experiments is the NV center. NV centers are vacancies adjacent to a nitrogen atom, present in a carbon lattice [1, 3]. For this project the carbon lattice was diamond, and as such diamonds containing NV centers we're used. An illustration of an NV center with a carbon lattice is given in Fig 1.

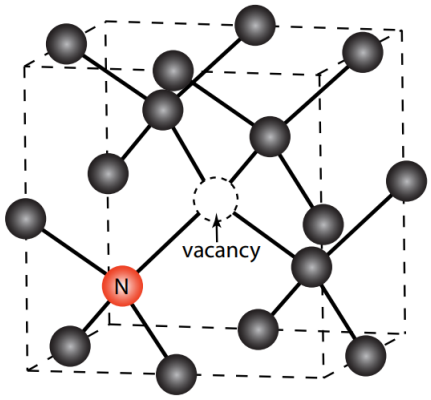

FIG. 1: This is a schematic of a Nitrogen Vacancy located inside a diamond carbon lattice. As per defination it is defined by being a vacancy adjacent to a nitrogen atom [4]

The quantum experiments to be run prior to the Covid-19 pandemic, that halted experimentation as parts of project during the Winter semester 2020, were measuring the red fluorescence emitted NV centers and magnetic imaging using the red fluorescence, measuring the ODMR dip and confirming magnetic sensing properties by using a continuous wave (CW) and RF power, broaden the ODMR dip by increasing the applied RF power, and confirm a steady state ratio of NV centers by saturating the diamond samples with green laser power. These experiments we're halted, as a result of the pandemic, and as such this report will

focus on the expected behavior of the system, as well as the progress of this project up to the pandemic causing campus closure.

II. BACKGROUND

Color centers are fluorescent lattice defects that consist of one or multiple impurities in the forms of atoms or vacant lattice sites within a crystal. These defects can be uniquely identified by their optical emission and absorption spectra. Fluorescent lattice are responsible for the typical coloration of diamond gemstones, and as such several hundred defects have been identified [2]. Today most diamonds produced today are consumed by industrial applications, as the material has superb mechanical hardness, heat conductivity and optical transparency [2, 5]. Among these impurities nitrogen-vacancy (NV) defects, show magnetic and quantum behavior up to room temperature. As such spurred by advances in single-molecule fluorescence, the detection of electron para-magnetic resonance (EPR) from a single NV defect was reported in 1997 [2]. This formed the basis of Optically Detected Magnetic Resonance (ODMR) techniques as ODMR combines EPR with measurements of fluorescence, phosphorescence and absorption [6], which allows magnetic interactions to be transferred into the optical domain [4, 6].

Diamonds containing NV centers are synthesized in 3 primary forms nanocrystals, thin films and bulk crystals[2]. For this project nanocrystals and thin films were to be used. There are two types of nanodiamonds used in experimentation, detonation nanodiamonds (DNDs), and nanodiamond powders. DNDs are synthesized by controlled denotations of TNT-like explosives in a closed vessel, these types of nanodiamonds have highly attractive properties for biological applications for their small size [2]. The nanocrystal used in this experiment was powder nanodiamonds, powder nanodiamonds is obtained by grinding large crystals to sub100 nm-sized particles, and are selected for by using centrifugation and dynamic light scattering [2] and are typically much purer than DND's. Current particle that are commercially available have median particle sizes of 15 nm, this is shown in 2. The nanodiamond particle sample used in this project had an average particle size of 100 nm.
Now thin film single crystal diamond plates with NV centers are synthesized with though high-pressure-high-temperature synthesis [2] or, by chemical vapor deposition (CVD). Plate

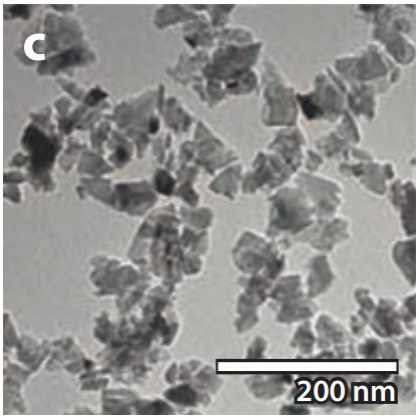

FIG. 2: This is an image of nanodiamonds, these nanodiamonds have a mean size of 15nm, however this project will use nanodiamonds with an average length of 100nm[2]

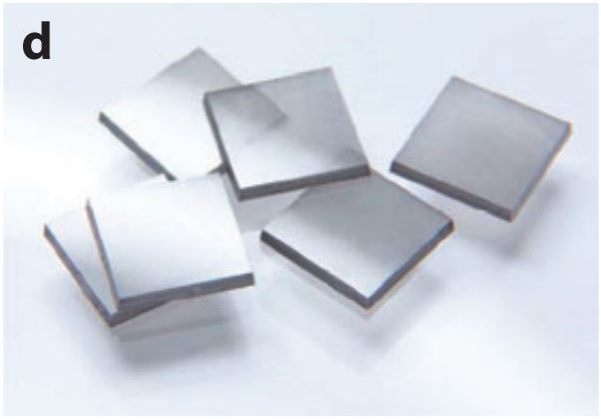

FIG. 3: These are thin film plate diamonds created by CVD, the samples used in this experiment contain similar thin film diamonds. [2]

dimensions up to 10 nm have been realized [2]. Large millimeter thin films can easily achieve the highest material quality with very low defect concentration[2], thus are highly desirable for ODMR experiments, as it would have high quantity of NV centers, while minimizing other impurities. The sample we use is a millimeter thin film plate diamond. An image, illustrating our sample is given in Fig 3.

The detection of EPR from a single NV defect triggered intense research efforts in the fields of quantum information science, causing the NV center to become an iconic model system. In project [2], NV centers formed the center piece of the ODMR system being built and investigated. An NV center can be found in three different charge states; positive charge state (NV^+), a negative charge state (NV^-) and a neutral state (NV^0). In the diamond samples used in this project, had a majority of its NV centers be in the negative state NV^-, the minority that wasn't in this state was in ground state (NV^0), with extremely small contributions from the positive state (NV^+). A schematic of a neutral state (NV^0), and negative state (NV^-) are given in the Figs 4, 5.

The naonodiamond and thin film samples chosen that contains a majority of its NV centers in a negative state (NV^-) was chosen because, it exhibits a strong ODMR signal [4], and is the only state that is magneto-optically active and as such all ODMR type experiments using NV centers use the negative ($NV-$) state. From here, the negative state of the NV

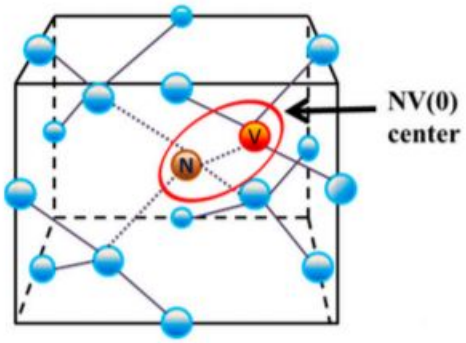

FIG. 4: This is a schematic of the neutral state of NV^0, where an extra electron is not present, hence the charges are balanced [5].

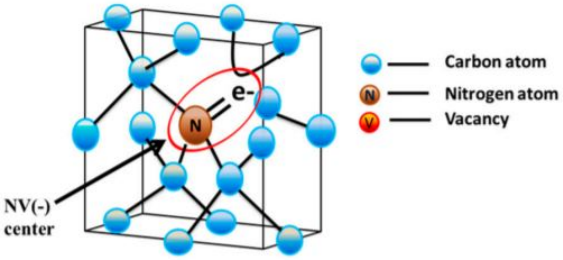

FIG. 5: This is a schematic of the negative state of NV^-, where an extra electron is present, hence the charges are overall negative with a charge of -1 [5].

center (NV$-$), shall simply be known as the NV center. The NV center has 3 electronic levels including a ground state of symmetry $|g\rangle$, an excited state of symmetry $|e\rangle$ and a metastable singlet state that involves two levels of symmetry $|s\rangle$ [2, 6]. The ground and excited states are further split into three spin sub-levels. These are given by the magnetic spins $m_s = |+1\rangle, m_s = |-1\rangle, m_s = |0\rangle$ [2, 4, 7]. Due to axial symmetry of the NV center the two $m_s = |\pm 1\rangle$ are degenerate and the $m_s = |0\rangle$ state is lower, this is illustrated in Figs 7,7. Now the referring back to Fig 7, it can be seen that energy difference between the between spin sub-levels is D = 2.87 GHz for the ground state, and D = 1.42 GHz for the excited state, where D is the so-called zero-field splitting[2]. The zero-field splitting is illustrated in Fig 8.

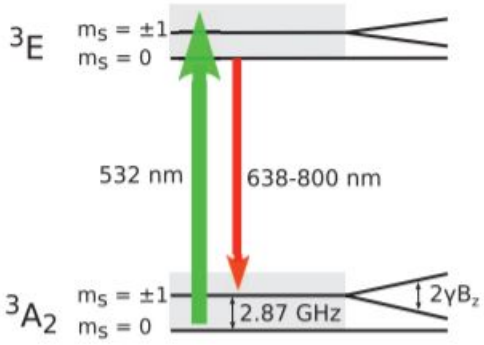

FIG. 6: Illustration of the 2-level system which allows NV^- to be opto-magnetically active. The green arrow indicates the wavelength used to excite NV center to the $|e\rangle$ state from the $|g\rangle$, where as the red-arrow shows the wavelength range for the photon emitted from the $|e\rangle$ state to the $|e\rangle$ state[8].

The zero-field splitting is the property of the NV center that allows ODMR to be used. This is because as shown in Fig 8, in the presence of a magnetic field B_z, the energy difference between the spin states $m_s = +1$ and $m_s = -1$ is equivalent to $2\gamma B_z$, where γ is the magnetic field coupling coefficient, which is equivalent to $28GHz/T$[2]. As such

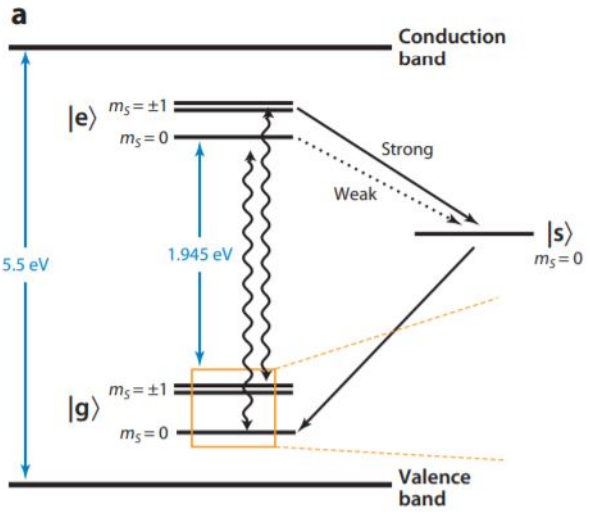

FIG. 7: Energy levels for NV center[2]. The yellow dashed lines zoom into the energy levels of the spin sublevels, and are expanded upon in Fig 8. The $|e\rangle$ is the excited state, $|g\rangle$ is the ground state and $|s\rangle$ is the metastable singlet state, which allows non-radiative transitions.

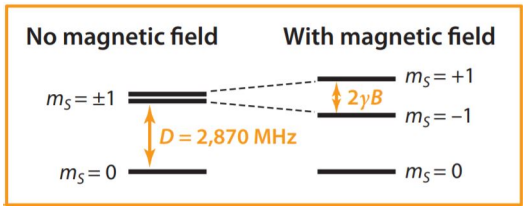

FIG. 8: Expanded Zoom in of the Energy differences between sublevels in the NV center, for both no external magnetic fields and external magnetic fields. If an external magnetic field is present hyperfine/zero-field splitting will occur as shown. [2]

when the $m_s = |+1\rangle$ state degenerates into a $m_s = |-1\rangle$ state, a photon with the frequency $2\gamma B_z$ is emitted. As such this allows magnetic interactions detected to be transferred into the optical domain, forming the basis for ODMR techniques [2, 8].

This series of experiments aim to firstly observe red fluorescence emission, and use it for magnetic imaging, produced from NV center power saturation resulting a green laser continuously illuminating the NV center. This is to be followed up by using the NV centers to perform ODMR with the use of RF(radio frequency) power, by measuring a dip in the fluorescent intensity measured as a result of up to 30% of the states excited states of NV center de-exciting using the non-radiative path, as shown in Fig7. this is to be followed up by the broadening of the ODMR curve by varying the RF power provided. Finally the NV centers are to be saturated with green laser power, and their output measured, to determine the ratio of NV$-$ centers to NV^0 centers.

Red Fluorescence is produced by the de-excited radiative transition between the excited state ($|e\rangle$) to the ground state $|g\rangle$. This is shown in Fig 7 and Fig 6. The red fluorescence when produced will form a spectrum that ranges from the wavelengths (638-800) nm [2, 4, 8]. This light can be utilized to view the particles producing them or measured as intensity in order to produce a spectrum. An illustration of the spectrum is shown in Fig 9.

The ODMR dip that occurs when RF power is

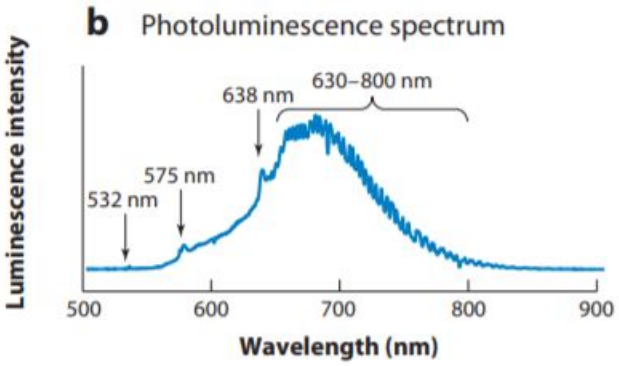

FIG. 9: Theoretical Photoluminsence spectrum that should be emitted by an NV center upon de-excitation [2].

applied to diamonds in order to allow ODMR to occur occurs because, when an RF power of 2.87 GHz is applied in conjunction to a continuous wave (CW) provided by a laser which has a wavelength less than 640 nm [2, 4], that allows continuous excitation, and thus fluorescence emission. Now as 2.87 GHz is the energy difference between the $m_s = |\pm 1\rangle$ and $m_s = |0\rangle$ sublevels in the ground state ($|g\rangle$). As such when applied if any state de-excites to an $m_s = |0\rangle$ state in the ground state ($|g\rangle$), it is excited up to the $m_s = |\pm 1\rangle$ in the ground state ($|g\rangle$), prior to being excited to the $m_s = |\pm 1\rangle$ in the excited state ($|e\rangle$), as shown in Fig 7. Now when the $m_s = |\pm 1\rangle$ in the state $|e\rangle$ de-excites, it may de-excite in one of two ways, the radiative path, or the non-radiative path. The radiative path is defined by the path $|e\rangle, |m_s = \pm 1\rangle - - > |g\rangle, |m_s = \pm 1\rangle$ as shown in Fig 7, in which case a photon will be emitted. The non-radiative path is defined as $|e\rangle, |m_s = \pm 1\rangle - - > |s\rangle, |m_s = 0\rangle - - > |g\rangle, |m_s = 0\rangle$ shown in Fig 7, where if this path is taken, a photon will not be emitted. The state will de-excite in the non-radiative path 30% of the time [2], as a result the flourescence dip would be up to 30%. This is shown in Fig 10. As such, if an RF power of 2.87 GHz is applied, theoretically the dip in the fluorescent intensity levels, up to 30% maybe caused.

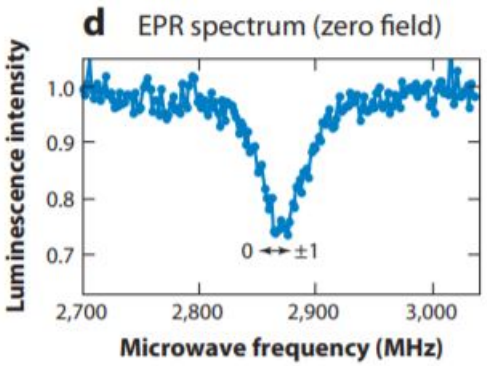

FIG. 10: Theoretical ODMR dip that should occur, as a result of non-radiative transitions[2].

The width of this dip is however determined by the relaxation or de-excitation time of NV centers [9]. The de-excitation time from $|e\rangle - - > |g\rangle$ for the thin film diamonds is 13ns, while 25ns for the nano-diamonds [2]. The de-excitation times form the basis of the frequency at which the states change, this state is known as the Rabi flopping frequency($\Omega_{i,j}$)

[10]. For an incident light field that is not at the exact resonant frequency of the transition, the generalized Rabi frequency equation given in equation 1, dictates rabi flopping of the sample. This because, a detuning constant (Δ) is introduce, which will excite the state to slightly above that of the resonant frequency [9]. This causes the states to excite and de-excite slower, the larger the detuning constant is. This causes the FWHM of any dip caused by this, to broaden provided the detuning constant (Δ), as defined 2 [9, 10]. Thus the larger the RF power applied is, the larger the detuning constant should be, and thus the larger broadening of an FWHM caused by Rabi flopping should be, this is illustrated in Fig 11 for the specific ODMR case, and in Fig 12.

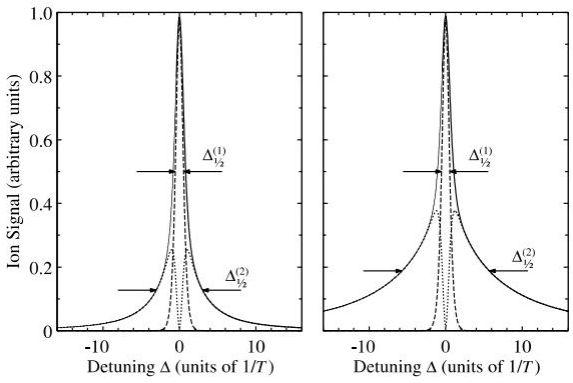

FIG. 11: Generalized FWHM broadening due to the occurence of detuning Δ [9]

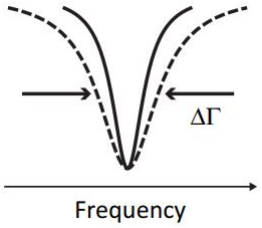

FIG. 12: ODMR broadening that should occur as a result of increased RF power where,$\Gamma = 2\Delta$, [11]

$$\tilde{\Omega_{i,j}} = \sqrt{\Omega_{i,j}^2 + \Delta^2} \tag{1}$$

$$\Delta = \omega_{light} - \omega_{transmission} \tag{2}$$

Now the final experiment will verify the NV^-:NV^0 ratio, during fluorescence saturation due to green laser power. This experiment will seek to establish that the ratio of NV^-:NV^0 is dependent upon photon incident energy, and thus the wavelength of the photon, and not the rate at which the photons are striking the NV centers [12]. This is because, the recombination rates for the NV^- and NV^0 centers depends energy of the photon striking the vacancies [12]. As such, at a given wavelength, the ratio of NV^-:NV^0 should form a steady state, with wavelengths less than 540nm having NV^-:NV^0 above 70% in the favor of NV^-. Two steady states for continuous waves emitted by lasers of wavelengths 560nm and 593nm are shown in

Fig 13.

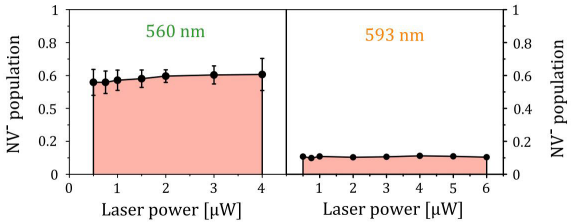

FIG. 13: NV steady state ratio's and their relationship to laser power applied [12].

III. CONTEXT AND METHODOLOGY

The first part of this project revolves around being able to built a cost effective ODMR set. A schematic for this of the system is shown in Fig 14.

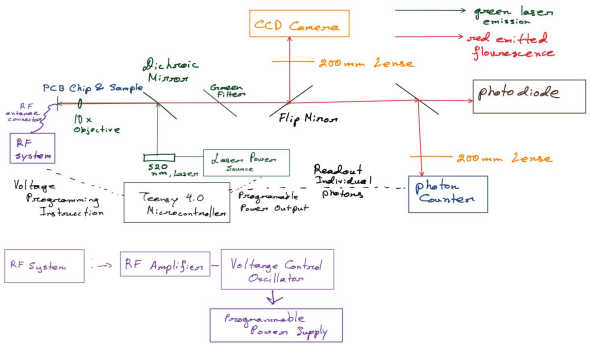

FIG. 14: This is the schematic that was designed and used to build the ODMR system in this project.

This schematic revolves around the sample, being place on a PCB and connected to an RF system to allow ODMR to be performed. Once a RF power system (shown in purple) is connected the the sample, mirrors can be used guide green laser power to it. Once the green laser power excites, it should emit red fluorescence, being emitted in the opposite direction from which the green laser came from. To analyze solely the red fluorescence being emitted by the NV center, a green light filter should be put in the path of red light as shown in the schematic in Fig 14. This will filter an erroneous green light that may have been reflected on to the path of the red fluorescence, leaving only the red fluorescence; this will allow the 4 experiments slated for this project to begin.

The 1st experiment revolves around measuring the red fluorescence emitted NV centers and magnetic imaging using the red fluorescence; to start this experiment, the red fluorescence should first be reflected to the ccd camera to begin magnetic imaging, while the ccd camera is interfaced with a computer. This should allow one to see the particles responsible for the fluorescence emission, verifying magnetic imaging capabilities. Once that is completed, the red fluorescence should be reflected towards the photodiode. This allow the measurement of red flourescence intensity to be measured. One should find a photospectrum similar to

the one in Fig 9. The photo-diode will report back in volts, and depending on which model, there will be a coefficient that will allow the direct conversion into wavelength detected. The model that was to be used in this experiment was a PDA36A2 from thorlabs. The coefficient varies from wavelength to wavelength according to the data-sheet, and thus must be numerically analyzed, which is not possible in this theoretical paper due to the pandemic.

The second experiment could begin by turning on the RF system connected to the sample and program in a range linear of frequencies with using the Teensy 4.0, connected to the RF system. In this case 2.87 Ghz should be in the middle of array programmed that is being fed into the sample. As the RF powers sweep the sample in a pre-programmed fashion, the red flourescence can be directed to either the photodiode or photoncounter. If one directs the red flourescence towards the photodiode, a dip in the intensity at 2.87 Ghz similar to Fig 10 should be seen. If one directs the red flourescence towards the photoncounter, a dip in the photon counts/sec should be seen and should resemble the dip in Fig 10. This will serve to confirm the opto-magnetic properties of the NV center [2, 4], and verify the quantum transitions that occur in the sub-levels due to the RF power being applied, as should in theory.

. The third experiment can be run by increasing the RF power being applied, this can also be done through the Teensy 4.0. As the detuning constant is defined as Δ in equation 2, one should increase the pre-programmed sweep time on the Teensy 4.0 using C++ as it should be interfaced with your computing device. As such, this will serve to increase the duration the RF power is applied onto the sample, thus increasing the RF power felt by the sample. This will cause ODMR broadening. Same procedure for the ODMR dip can be applied here, and the flourescence can be redirected to both the photoncounter and photodiode, one should see the ODMR dip broaden compared to when the sweep time was less, for both counts and intensity.

Lastly, to measure the saturation of NV centers due to green laser power, one can turn of the RF systems and simply shine the green laser on to the sample and start modulating its power output using the power source and Teensy 4.0. As the red-flourescence is directed to the photo-diode to measure output of its intensity, one should notice a constant relation

between the power being outputted by the sample and power of the laser, indicating the power of the laser past 1μW [12] has no effect on the ratio of NV^-:NV^0, confirming a steady state ratio for the sample.

These experiments should be interfaced with an computing device that can support Arduino programming language IDE and C++; as all signals being sent to the RF system, photon counting system, and laser power modulation can be programmed in by using a Teensy 4.0 micro-controller. A Teensy 4.0 micro-controller (shown in Fig 20) or higher should be used in this experiment (as of writing this, the Teensy 4.0 is the fastest micro-controller that can be found on the market). The photo-diode can be linked Teensy 4.0 as well, or an oscilloscope, where as the ccd camera directly interfaces with a computing system which runs an OS system of higher than windows XP. This will effectively allow the experimenter to interface the ODMR system built with his/her computing device, achieving the goal of interfacing a cost effective ODMR microscope with modern computing technology. The components required to build this system, the estimated cost of each component, and the total cost spent prior to the pandemic to build this system is shown in Table I.

TABLE I: This table contains the parts, part name, price, and quantity required to build this experiment. It also contains whether these items were present prior to the begining of the experiment. If they were, they were not included in the final cost spent.

Green laser				
Item	Part Number/Information to obtain it	Price	Quantity	In Lab
Green laser collimator	LTN330-A	252	1	No
Green Laser Diode (50mW, 520nm)	PL520 - 520	81.7	1	No
Diode socket	S038S	4.2	1	No
Strain relief cable	SR9F-DB9 - ESD	57.63	1	No
Current source	MLDEVAL	133.1	1	No
Power supply Cable (5 V DC)	Use a wall plug for thi	12	1	Yes
Thread adapter	AD15F - SM1	33	1	No
Post	TR075V	12.85	12	Yes
Mount cage	CP33/M	16.89	1	No
post holder	PH3-P5	42.35	12	Yes
Green laser excitation and red collection				
Item	Part Number/Information to obtain it	Price	Quantity	In Lab
Dichroic mirror	DMLP550T	122.28	1	No
M4 posts	M4 post - Thorlabs	12.87	12	Yes
Kinematic mount for Dichroic	KM05/M	40	1	Yes
Flip mounts for mirrors	TRF90/M	89	3	Yes
mirror mount	FMP1/M	17	12	Yes
Mirrors	ME1-G01	15	12	Yes
Objective mount	OMR/M	30	1	No
10x objective	RMS10X	382.35	1	No
PhotoDetector	PDA36A2	347.36	1	No
Mount for lens of photodiode	SMR1/M	20	1	Yes
Lens for Photodiode	LA1509-B-ML	48	1	Yes
Lens for CCD	MVL100M23 - 100 mm EFL	198	1	Yes
Long Pass Filter	FEL0600	80.62	1	No
Mount for filter	LMR1/M	16	1	Yes
PhotoDiode BNC to pins	Teensy Header Kit	1.5	1	No
Post holder	PH3-P5	42.35	12	Yes
Novelty				
Items				
PhotoCounting Module	SPCM-AQRH-10	3,647.87	1.00	Yes
Teensy 4.0	Teensy 4.0 Development Board	19.95	1	No
CCD camera	Logitech QuickCam Fusion	189	1	Yes
Microwave Excitation				
Item	Part Number/Information to obtain it	Price	Quantity	In Lab
Copper wire (20-40 um) with connectors	Get it from any cable	0	2	Yes
RF Amplifier	ZRL-3500+	139.95	1	No
antenna connector (SMA edge connec	phenol RF - 901-1051	12	1	No
ble (from Amp to RF antenna, RF antenn	FL086-12SM+	17	1	No
Co-axial cable (From RF source to Amp	141-4SM+ (0.1 m)	9.49	1	No
4dB attenuator	VAT-4+	31.95	1	No
Attenuator (To close the RF circuit)	BW-S10W5+	48	1	No
Voltage Controlled Oscillator	ZX95-3250-S+	90.95	1	No
Sample				
Item	Description	Unit Price	Quantity	In Lab
Diamond Sample	SC Plate Type Ib 3.0x3.0mm, 0.30mm thick, <100>, PL	190	1	No
NanoDiamond Sample	Fluorescent nanodiamond, Nitrogen vacancy >900 NV/particle, 100 nm avg. part. size (DLS), 1 mg/mL in deionized water, hydroxylated	377	1	No
Total Cost Counting Non-Present Lab equipment		2478.92		

Elaborating on progress and objectives achieved prior to the pandemic, a cost efficient ODMR microscopy system was built up in the

junior science labs located in the basement of Science B and the University of Calgary. A few pictures of ODMR microscopy system prior to the pandemic causing campus closure are shown in Figs 15 and 16. Notable technical

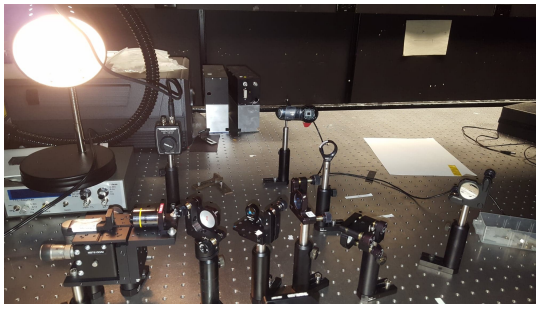

FIG. 15: Physical picture of the built ODMR system from the front end.

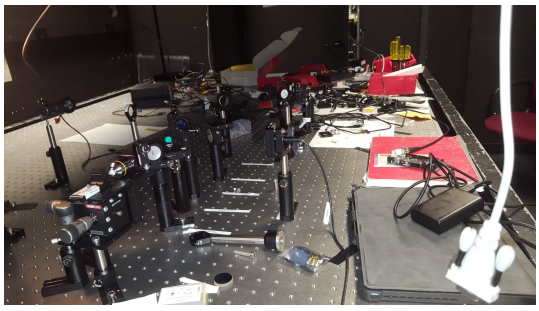

FIG. 16: Physical picture of the built ODMR system from the left hand side

achievements that verified the functionality of this system, include being able able to detect the RF power of 2.87 Ghz being produced by RF amplifier ZRL-3500+, as shown in Fig 17. This was followed up by being able to detect single photons with both the Teensy 4.0 (a good image could not be taken, prior to campus closure), and oscilloscope. The signal of a single photon is shown in Fig 18, on the screen

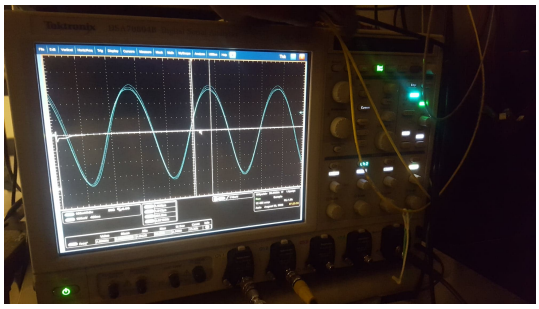

FIG. 17: RF pulses of 2.87 GHz being generated by ZRL-3500+, and being displayed on an oscilloscope.

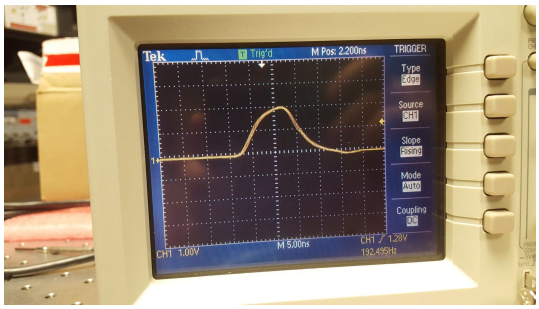

FIG. 18: Signal generated by a single photon captured when counting the darkcounts prior to the experiment, in order to deduct the background noise from actual flourescence counts using the photon counter.

of an oscilloscope with a resolution of 5ns. This piece of information allows the understanding the photon counting process of the Teensy 4.0 should've worked if not for the pandemic, as the Teensy 4.0 has a resolution of 2ns.

The PCB boards as well as the electrical connections to the sample we're shouldered on, as shown in Fig 19, and the samples of nanodiamonds and thin film diamonds would've been attached to the glass slide on the PCB chip shown in Fig 19, and inserted right behind

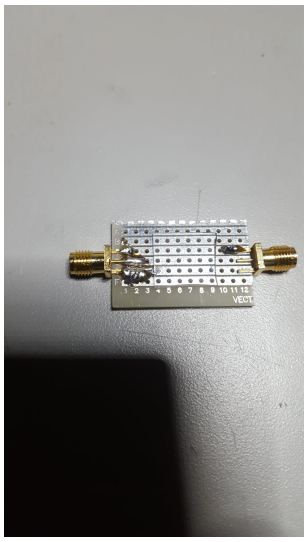

FIG. 19: PCB chip engineered to contain the samples for experimentation

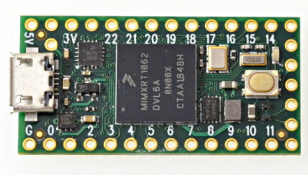

FIG. 20: Picture of the Teensy 4.0 microcontroller that allows computer interface with the ODMR system.

the 10x objective lens, thus making ODMR system ready for testing, as all other systems we're tested and ready. Experiments could not be carried out because the date at which the experimentation was scheduled to begin March 16^{th} 2020, coincided with campus closure due to the pandemic.

IV. THEORETICAL RESULTS

In light of the lack of the experimentation due to the Covid-19 pandemic, the expected results and behavior of the ODMR experiments will be analyzed. The behavior of the system depend heavily on the specifications of the samples being used, as well as the volume of sample being excited. Using the information provided the manufacture of the objective lens, which focuses the laser onto the sample, the excitation volume of nanodiamond sample and thin film diamond sample can be calculated. The excitation volume is defined as equation 3 as shown by Olympus on their website [13].

$$ex_{vol} = r_{laterial}^2 * r_{axial} \tag{3}$$

$$r_{laterial} = \frac{0.4\lambda}{NA} \tag{4}$$

$$r_{axial} = \frac{1.4\lambda\eta}{NA^2} \tag{5}$$

The NA for our objective was 0.25, our wavelength used for this experiment was 520nm, the index of refraction for water and diamond is $\eta = 1.33$, $\eta = 2.44$. Thus the excitation volume for our nanodiamond and diamond sample are:

$\text{ex}_{vol-nano} = \frac{0.4\lambda}{NA}^2 * \frac{1.4\lambda\eta}{NA^2}$

$ex_{vol-nano} = \frac{0.4(520nm)}{0.25}^2 * \frac{1.4(520nm)(1.33)}{(0.25)^2}$

$ex_{vol-nano} = 2.681 * 10^{-12} cm^3$

$\text{ex}_{vol-diamond} = \frac{0.4\lambda}{NA}^2 * \frac{1.4\lambda\eta}{NA^2}$

$ex_{vol-diamond} = \frac{0.4(520nm)}{0.25}^2 * \frac{1.4(520nm)(2.44)}{(0.25)^2}$

$ex_{vol-diamond} = 4.918 * 10^{-12} cm^3$

Thus,

$\text{ex}_{vol-nano} = 2.681 * 10^{-12} cm^3$

$ex_{vol-diamond} = 4.918 * 10^{-12} cm^3$

The nanodiamond sample used in this project was procured from Millipore Sigma being the product number 900174, Fluorescent nanodiamond. It has the specification of its nanodiamonds being 100nm in mean size, each particle having 900 NV centers, with it being suspended in deionized water with density of 1mg/mL. Thus, the number of particles contained in this sample as well as NV center can be computed as follows:

The number of particles per cm^3 can be found by the following:

$$100nm - - > 10^{-5} cm$$

Thus, there is 1 particle every 10^{-5}cm

Thus every particles/mL or particles/mL;

$\text{n}_p = \frac{1cm^3}{1mL} * (1particle/(10^{-5} cm))^3$

$n_p = 10^{15}/mL$

$n_p = 10^{15}/cm^3$

This would indicate the number of NV centers for excitation volume for the nanodiamond is (assuming 70% of them are NV^- [12]:

$\text{n}_{NV} = 0.7 * 900 * n_p * ex_{vol-nano}$

$n_{NV} = 1.689 * 10^6 NV^- centers$

The thin film diamond sample used in this project was procured from element 6 a subsidiary of the De Beer Group. It's item number is 145-500-0266, and it is a SC Plate Type Ib 3.0x3.0x0.3mm <100> PL thin plate fluorescent diamond. It has a nitrogen concentration of >200ppm. From this source [14], as the same diamond was used its NV concentration was assumed to 2ppm. The data-sheet provided by element 6 indicated particle density is given by $n = 1.77 * 10^{23}/cm^3$, as such the number NV centers in the excited volume of the diamond assuming 70% of them are NV^- [12]:

$\text{n}_{NV} = 0.7 * 2 * 10^{-6} * n * ex_{vol-diamond}$

$n_{NV} = 1.218 * 10^6 NV^- centers$

Thus the total usable NV centers for the nanodiamond sample is $n - nano_{NV} = 1.689 * 10^6 NV^- centers$, while thin film diamond sample had a total usable $n - diamond_{NV} = 1.218 * 10^6 NV^- centers$. Now radiative lifetimes for excited states in bulk and thin plate diamonds is approximately

13ns [2] and approximately 25ms in nanodiamonds [2]. This is due to differences in index of refraction (η). This means if excited, the nanodiamonds and thin plate diamond sample would respectively produce $6.756 * 10^{13}$ counts/sec and $9.369 * 10^{13}$ counts/sec. As each count represents a fluorescent photon, the energy range (2.480*10^{-19} Joules- 3.115*10^{-19} Joules) can be calculated using planks energy formula given by equation 6.

$$E = \frac{hc}{\lambda} \tag{6}$$

Multiplying the energy range of a single count (photon) with the count rate, the power emission ranges for the diamond samples can be deduced. Doing this it can be found that the power emission ranges for the nanodiamond samples is (21.011μW - 16.755μW), while the emission ranges from the thin film diamond samples should (29.150μW - 23.250μW). Thus to summarize the sample analysis, it was expected that the nanodiamond sample would produce a count rate of approximately $6.756 * 10^{13}$ counts/sec, and an emission range of (21.011μW - 16.755μW), while the thin plate diamond sample would produce a count rate of $9.369 * 10^{13}$ counts/sec, and a power range of (29.150μW - 23.250μW).

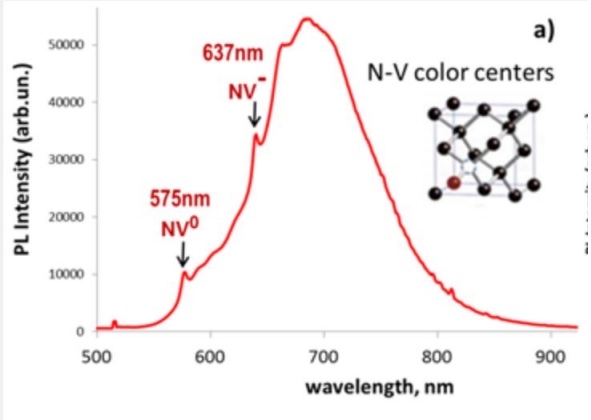

FIG. 21: The theoretical photoluminescence spectrum produced by the photo nanodiamond sample, as provided by Sigma. The thin film diamond sample should also produce a photoluminescence spectrum as the NV centers within the diamond are quite similar in counts.[Taken from Sigma product page]

Thus in the context of the experiments, it was expected that the red flourescence photospectrum would be something similar to the Figure 21, as indicated by the manufactures Sigma, and Element 6.

The manufactures indicated that the ODMR dip, would only have a contrast of (2-6)%, because of impurities present in the samples which are not nitrogen. For instance on the element 6 page for the item, it is specified it is 2% boron and as such an ODMR dip of (2-6)% as shown by Fig 22. . This dip can be modelled by a Lorenzian fit, this is because it is the

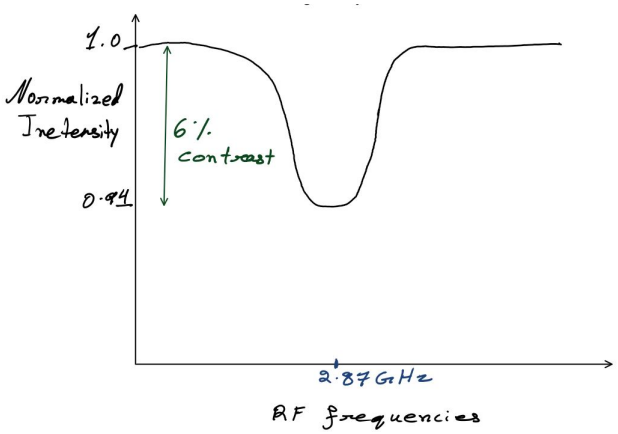

FIG. 22: Theoretical ODMR dip caused by non-radiative paths taken with both samples

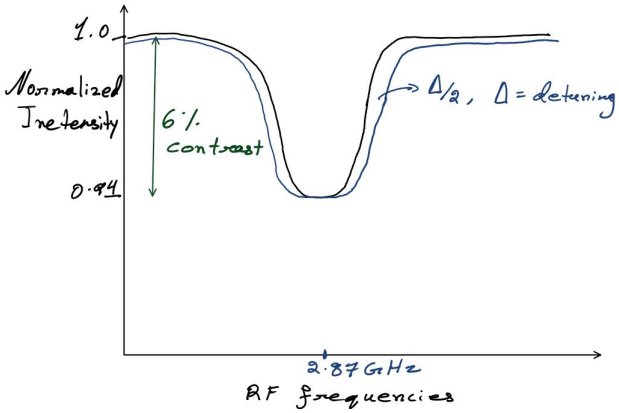

FIG. 23: Theoretical ODMR broadening by the detuning constant Δ within both samples.

distribution ratio of two independent normally distributed variables, with a center mean [15]. These 2 normally distributed variables are RF power, and normalized intensity or normalized photon counts, when the photon counter is used for experimentation.

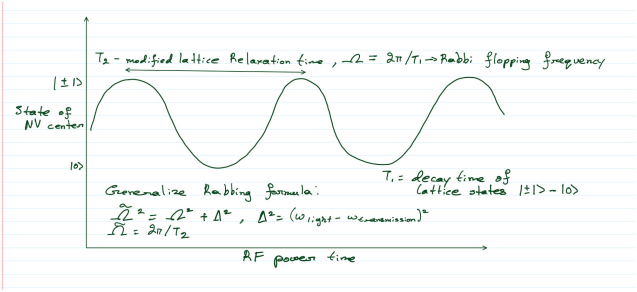

FIG. 24: Relation between the sublevels and $|\pm 1\rangle$ and $|0\rangle$ and the Rabi flopping frequency.

It is anticipated that when the ODMR dip produced by the samples, is broadened by RF power it will broaden by a factor of $\Delta/2$, as shown in Fig 23. This is because of the generalized Rabi flopping frequency increasing due to $\Delta/2$ as shown in equation 1. This will cause the de-excition times between the $m_s = |\pm 1\rangle$ and $m_s = |0\rangle$ in the samples to decrease. It is expected this will cause the FWHM of the ODMR dip to broaden.

Now the theoretical results for the last experiment, NV flourescence is shown in Fig 25. It shows that the power emissions from the samples should stay constant, this is because wavelength here (520nm) does not change, and only its power is being modulated. This is expected to keep the ratio of NV^- : NV^0 centers constant, at a 3:1 ratio, thus causing the power emitted to match with the power emission range for the samples.

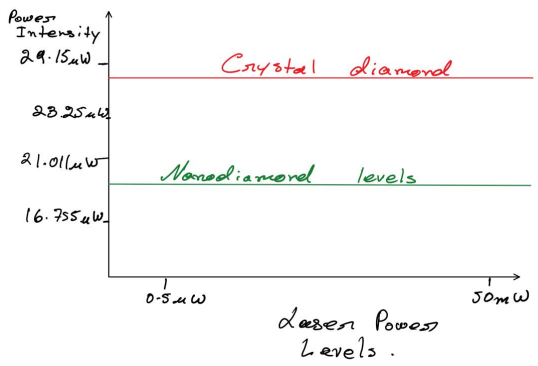

FIG. 25: Theoretical Power saturation output based on the samples.

V. ANTICIPATED RESULTS AND PROJECT SUMMARY

Comparing the anticipated results to literature, it is quite consistent. The manufactures floures-cence from both Sigma and Element 6 match fluorescent observations from [4] as shown in Fig 26, and [2] are shown in Fig 9, thus it reasonable to assume that the flourescence photospectrum should've matched if the experi-ment was carried through.

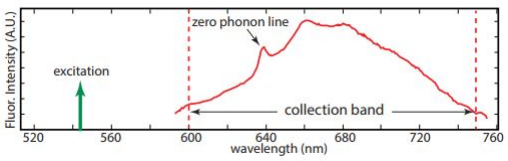

FIG. 26: Observed Photoluminescence spectrum in [4]

Comparing the ODMR dip and broadening compared to previous literature, the previous results do theoretically match ours, however most experiments an external magnetic field to hyperfine/zero-field split the $m_s = -1$ and $m_s = +1$ to perform hyperfine resolution magnetic imagine [7, 16], as the resolution of the photons generated in this manner allow optical wavelength resolution imaging. As such it is anticipated, in ODMR dip in this experiment will not be split, similar too Fig 10. This is not the case in [7], as a minor split between the states at an application of 0mT is shown in Fig 27[7]. This would indicate that a minor magnetic field was present during the publication of this paper, thus causing the split in the state, as the γ coefficient = 28 GHz/T [2]. This would indicate a very small not measured magnetic field split the state up, a similar result would happen to this experiment if a non-measured magnetic field was present. This similarly present in [4] as in both Figs 28, 29, both thin plate and nanodiamond samples have this same feature. Theoretically, our dip should be smooth similar to Fig 10, however it is more likely that practically the results would match these 2 papers, as a minute magnetic field that wouldn't be measured could be present.

Now, there could be no literature found

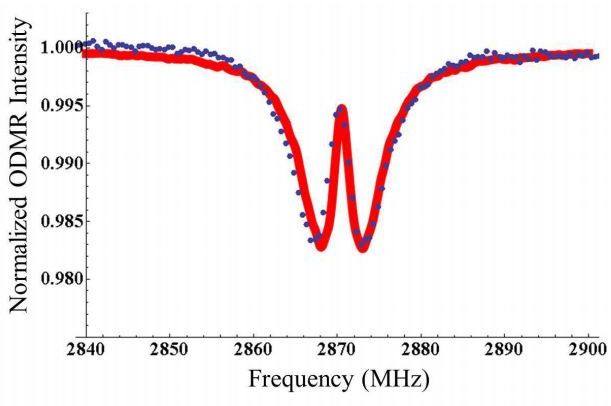

FIG. 27: Observed ODMR dip in [7].

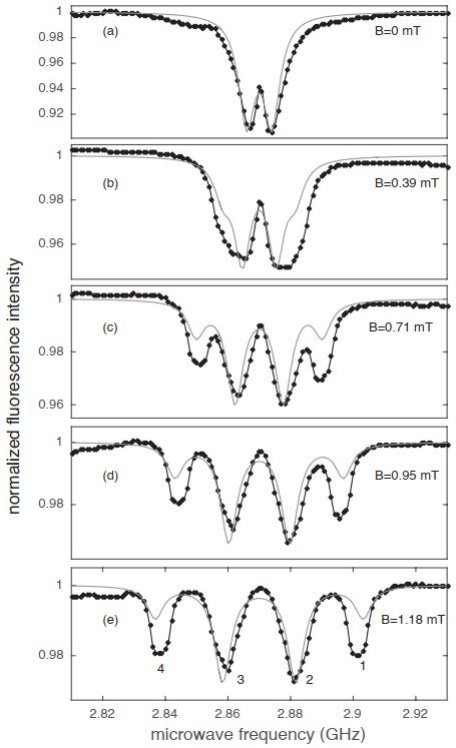

FIG. 28: Observed ODMR dips for nanodiamonds at a variety of external magnetic fields in[4].

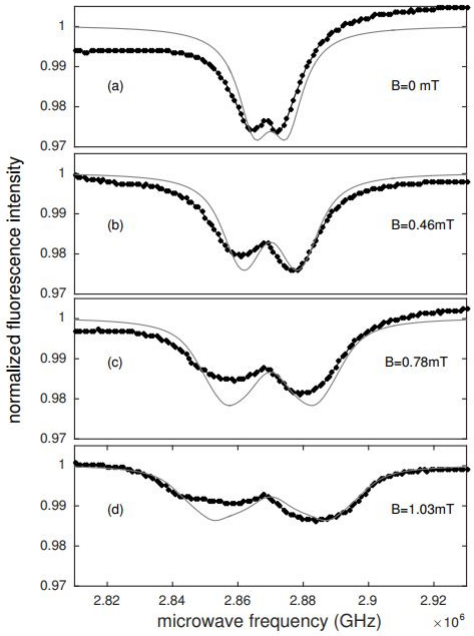

FIG. 29: Observed ODMR dips for thin plate diamonds at a variety of external magnetic fields in Caption[4]

comparing non-magnetic split ODMR curve, that was being power broadened with RF power. As a result, a comparison between the magnetically split ODMR curve, that has RF power being applied to it and the hypothetical results will be conducted, in hopes to see if the general of the ODMR broadening is the same. In [16], we can see an ODMR curve that is being broadened by RF power, as shown in Fig 30. In [16], its being shown that the ODMR curve is being broadened by a factor of $2\omega_n$ (where ω_n is the transition frequency) indicating its detuning factor Δ is $4\omega_n$ as indicated in [9]. Using the defination of detuning in equation 2, it can be shown that RF power of $5\omega_n$ was applied the diamond sample in [16]. The behavior of this curve matches that of the theoretical ODMR broadening shown in Fig

23, as if an RF power of $5\omega_n$ applied in [16], it would match the predictions generated by the detuning constant (Δ). If an RF power of $5\omega_n$, was not applied there are other factors at play here that further affect the ODMR broadening, such curve becoming wider upon the application of an external magnetic field, due to hyper-fine splitting [2] of the sublevels $m_s = |-1\rangle$ and $m_s = |1\rangle$. This is observed in both nanodiamond and thin film diamond samples in [4]. In both cases RF power is not applied and they are shown in Figs 28, 29, indicating RF power is not the only factor when it comes ODMR dip broadening. As such it can be deduced if an RF power of $5\omega_n$ is not applied, then the difference would be made up by the fact a non-zero magnetic field is hyperfine splitting the states of the sample in [16].

Now comparing the final experiment to the final piece of literature [12], it can be seen in theoretical results in Fig 25 and results of previous literature Fig 13, have similar expected behavior. The difference in steady state ratios for $NV^- : NV^0$, would be due to the difference in wavelength as for this project a laser of wavelength 520nm was used as opposed to 560nm or 593nm as was in [12].

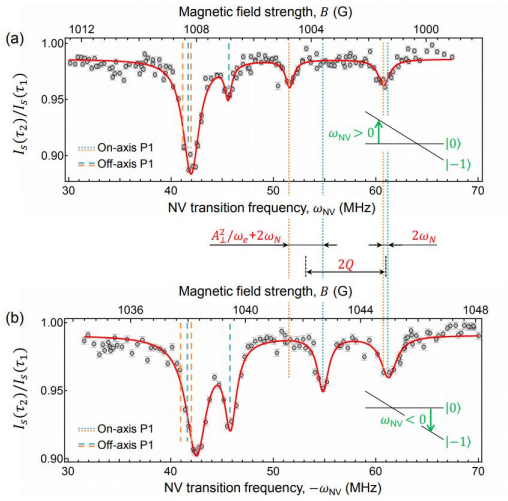

FIG. 30: RF and Magnetic Broadening of ODMR curves as observed in [16]

Thus overall the theoretical results discussed prior, matched the behavior of experiments from previous literature. The behaviors did not match exactly, and that is to be expected because there are slight differences between the experiments conducted within this project and previous literature, but the core physics do effectively check out.

Now summarizing the project, this project only met 1 of its objectives due to the covid-19 pandemic; the building of a cost of effective ODMR microscope that has the ability to interface with modern computing technology. The 4 experiments that we're scheduled to be conducted prior to the pandemic have their theoretical behaviors match previous literature, and as such it is reasonable to belief if this ex-

periment we're to have gone through, it would be successful; as the theoretical calculations predict it would.

VI. CONCLUSIONS

This project had the motivation of advancing the field of Magnetic Microscopy, by building a cost effective ODMR microscope that could perform quantum experiments, which would also be interfaced and integrated with modern computing technology. This would allow highly extreme quantum experiments to be run in a highly time efficient and cost efficient manner. This is due to two reasons, i) being able to build the ODMR set in under 2500 USD ii) the high levels of automation introduced by the Teensy 4.0 micro-controller. The expected behavior for this ODMR system also matches with previous literature, and as a result if this experiment ran it should have been a success. Therefore, if this experiment ran it would be able to perform a cheap but powerful magnetic microscopy due to the logitech fusion pro ccd camera used in the system, measure any power coming from the NV center using the photodiode, as well as count individual photons coming into the photoncounter due to Teensy 4.0. It would also be able to measure the red flourescence spectrum coming out the NV centers, the ODMR dip as a result of RF power, the ODMR broadening as a result of the increased application of RF power, as well as measure $NV^- : NV^0$ ratios by measuring the emitted flourescence. The projects main contributions to field would've been increased cost effectiveness, and experiment automation, and computer interfacing.

VII. ACKNOWLEDGEMENTS

First a big thank you to Dr.Paul Barclay for providing a plethora of resources in terms of knowledge, capital, space and patience for me to conduct this project.

Secondly, a HUGE thanks to Prasoon Kummar Shandilya, he's helped me with this project from day 1, whether it be wiring and shouldering individual wires, components or part assembly, this project would be basically impossible without him.

Third, I'd like to thank Ms.Marnie from the physics department for providing me with an office to conduct the experiment from, this experiment was sped up expotentially due to her, I can't thank her enough.

I would also like to thank Suzan and Dr.Wieser for providing me with the space to build the ODMR system, as well as conduct the experi-

ment.

I would also like to thank the Ucalgary Physics and Astrophysics department for supporting this ambitious Phys 598 project both academically and financially uofc physics department for providing monetary support.

I finally would like to thank you for taking the time to read this paper and about my project!

---

[1] M. Robinson, J. Ng, H. Zhang, J. Buchman, O. Shenderova, C. Haynes, Z. Ma, R. Goldsmith, and R. Hamers, "Optically detected magnetic resonance for selective imaging of diamond nanoparticles," *Analytical Chemistry*, p. 769, 2018.

[2] R. Schirhagl, K. Chang, M. Loretz, and C. L. Degen, "Nitrogen-vacancy centers in diamond: Nanoscale sensors for physics and biology," *Annual Review of Physical Chemistry*, vol. 65, pp. 83–105, Apr. 2014.

[3] Y. Matsuzaki, H. Morishita, T. Shimooka, T. Tashima, K. Kakuyanagi, K. Semba, W. J. Munro, H. Yamaguchi, N. Mizuochi, and S. Saito, "Optically detected magnetic resonance of high-density ensemble of nv centers in diamond," *Journal of Physics: Condensed Matter*, vol. 28, no. 27, p. 275302, 2016.

[4] H. Zhang, C. Belvin, W. Li, J. Wang, J. Wainwright, R. Berg, and J. Bridger, "Little bits of diamond: Optically detected magnetic resonance of nitrogen-vacancy centers," *American Journal of Physics*, vol. 86, pp. 225–236, Mar. 2018.

[5] A. Haque and S. Sumaiya, "An overview on the formation and processing of nitrogen-vacancy photonic centers in diamond by ion implantation," *Journal of Manufacturing and Materials Processing*, vol. 1, p. 6, Aug. 2017.

[6] P. Delaney, J. C. Greer, and J. A. Larsson, "Spin-polarization mechanisms of the nitrogen-vacancy center in diamond," *Nano Letters*, vol. 10, pp. 610–614, Feb. 2010.

[7] Y. Matsuzaki, H. Morishita, T. Shimooka, T. Tashima, K. Kakuyanagi, K. Semba, W. J. Munro, H. Yamaguchi, N. Mizuochi, and S. Saito, "Optically detected magnetic resonance of high-density ensemble of nv centers in diamond," *Journal of Physics: Condensed Matter*, vol. 28, no. 27, p. 275302, 2016.

[8] M. Simanovskaia, K. Jensen, A. Jarmola, K. Aulenbacher, N. Manson, and D. Budker, "Sidebands in optically detected magnetic resonance signals of nitrogen vacancy centers in

diamond," *Physical Review B*, vol. 87, no. 22, 2013.

[9] N. Vitanov, B. Shore, L. Yatsenko, K. Böhmer, T. Halfmann, T. Rickes, and K. Bergmann, "Power broadening revisited: theory and experiment," *Optics Communications*, vol. 199, pp. 117–126, Nov. 2001.

[10] M. Fox, *Quantum optics: an introduction*. Oxford Master Series in Atomic, Optical and Laser Physics, Oxford: Oxford Univ. Press, 2006.

[11] M. Fujiwara, Y. Shikano, R. Tsukahara, S. Shikata, and H. Hashimoto, "Observation of the linewidth broadening of single spins in diamond nanoparticles in aqueous fluid and its relation to the rotational brownian motion," *Scientific Reports*, vol. 8, Oct. 2018.

[12] N. Aslam, G. Waldherr, P. Neumann, F. Jelezko, and J. Wrachtrup, "Photo-induced ionization dynamics of the nitrogen vacancy defect in diamond investigated by single-shot charge state detection," *New Journal of Physics*, vol. 15, p. 013064, Jan. 2013.

[13] "confocal microscopy - resolution and contrast in confocal microscopy." `https://www.olympus-lifescience.com/en/microscope-resource/primer/techniques/confocal/resolutionintro/`.

[14] P. Kehayias, M. Mrózek, V. M. Acosta, A. Jarmola, D. S. Rudnicki, R. Folman, W. Gawlik, and D. Budker, "Microwave saturation spectroscopy of nitrogen-vacancy ensembles in diamond," *Physical Review B*, vol. 89, June 2014.

[15] D. Summers, S. Xue, and R. M. Thorne, "Calculation of the dielectric tensor for a generalized lorentzian (kappa) distribution function," *Physics of Plasmas*, vol. 1, pp. 2012–2025, June 1994.

[16] J. D. A. Wood, D. A. Broadway, L. T. Hall, A. Stacey, D. A. Simpson, J.-P. Tetienne, and L. C. L. Hollenberg, "Wide-band nanoscale magnetic resonance spectroscopy using quantum relaxation of a single spin in diamond," *Physical Review B*, vol. 94, Oct. 2016.